# Recovering 3D Shapes from Ultra-Fast Motion-Blurred Images

Fei Yu[1], Shudan Guo[1], Shiqing Xin[1], Beibei Wang[2], Haisen Zhao[1†], Wenzheng Chen[3]
[1]Shandong University [2]Nanjing University [3]Peking University

## Abstract

*We consider the problem of 3D shape recovery from ultra-fast motion-blurred images. While 3D reconstruction from static images has been extensively studied, recovering geometry from extreme motion-blurred images remains challenging. Such scenarios frequently occur in both natural and industrial settings, such as fast-moving objects in sports (e.g., balls) or rotating machinery, where rapid motion distorts object appearance and makes traditional 3D reconstruction techniques like Multi-View Stereo (MVS) ineffective.*

*In this paper, we propose a novel inverse rendering approach for shape recovery from ultra-fast motion-blurred images. While conventional rendering techniques typically synthesize blur by averaging across multiple frames, we identify a major computational bottleneck in the repeated computation of barycentric weights. To address this, we propose a fast barycentric coordinate solver, which significantly reduces computational overhead and achieves a speedup of up to **4.57**×, enabling efficient and photorealistic simulation of high-speed motion. Crucially, our method is fully differentiable, allowing gradients to propagate from rendered images to the underlying 3D shape, thereby facilitating shape recovery through inverse rendering.*

*We validate our approach on two representative motion types: rapid translation and rotation. Experimental results demonstrate that our method enables efficient and realistic modeling of ultra-fast moving objects in the forward simulation. Moreover, it successfully recovers 3D shapes from 2D imagery of objects undergoing extreme translational and rotational motion, advancing the boundaries of vision-based 3D reconstruction.*

## 1. Introduction

Estimating the shape of an object from image collections is crucial for numerous applications, including film production, gaming, and AR/VR. As a long-standing goal in computer vision and graphics, extensive research has leveraged geometric and learning-based priors for object shape recovery [5, 9, 11, 14, 22]. However, most existing methods focus on static objects or those with low-speed motion [4, 23, 43], leaving shape recovery of high-speed objects largely underexplored.

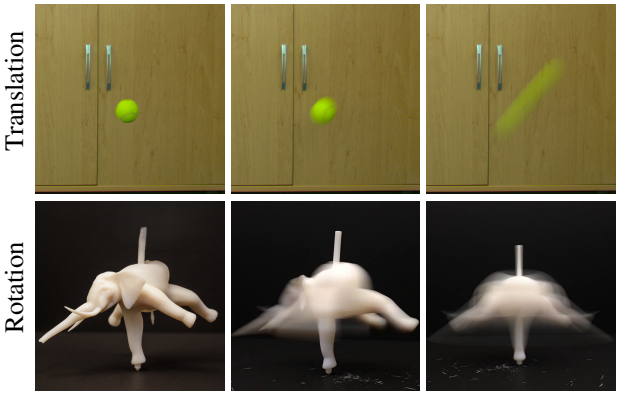


Figure 1. **Ultra-fast motion blur** is common in real-world scenarios. Top: A ball undergoing translational motion [32]. Bottom: A spinning top in rotation [1]. In this paper, our goal is to recover 3D shapes from the high-speed translational and rotational motion.

In this work, we investigate an extremely challenging question: Can we recover the shape of an object undergoing ultra-fast motion? Fast motion is prevalent in real-world scenarios, such as flying balls in sports, rotating machinery, or high-speed robotics. While reducing exposure time can mitigate blur, it often leads to extremely low signal-to-noise ratios in low-light conditions, making motion blur physically unavoidable in many practical scenarios. However, extreme motion blur severely distorts the object's appearance, often obscuring the underlying shape. As shown in Fig. 1, the object's shape is barely perceptible in the captured blurry images, making traditional multi-view geometry-based methods, such as Structure from Motion (SfM) [9, 11], ineffective. SfM-based techniques rely on sharp feature correspondences across views, but when motion blur obscures these features, shape recovery becomes highly challenging.

Alternatively, recovering 3D shape from 2D image collections can be formulated as an inverse problem, where the objective is to optimize the shape so that its renderings match the observed images [22]. Leveraging this paradigm, we formulate shape recovery under ultra-fast mo-

†Corresponding author.

tion as an inverse rendering problem, where both geometry and appearance are estimated by simulating the blurry process. Typically, motion blur can be approximated by rendering multiple static frames and averaging them [32–34, 39]. However, this method becomes computationally expensive for ultra-fast translational or rotational motions. As shown in Fig. 2, generating realistic motion blur under such conditions requires synthesizing and averaging over 50 individual static frames per blurry image, leading to excessive rendering costs and memory consumption.

We carefully analyze the computational bottleneck in motion blur synthesis. While a single barycentric computation is inexpensive, we identify that the repetitive calculation of these weights required for temporal integration becomes a primary source of inefficiency. This is because barycentric weights must be computed for every pixel with respect to all triangles, and the synthesis of motion blur further amplifies the computational cost by requiring these computations across all sampled frames, leading to a significant overhead. To address this issue, inspired by analytic motion approximation techniques [10], we propose a fast barycentric coordinate solver that significantly reduces computational complexity. By integrating this solver into our differentiable rasterization framework, our approach achieves significant speedup while preserving the accuracy of motion blur simulation. Furthermore, we reformulate the rendering process in a soft, fully differentiable manner, allowing gradients to propagate through motion-blurred images to the underlying 3D shapes.

With its differentiable capabilities, our framework enables 3D shape recovery through an inverse rendering pipeline: Beginning with an initial 3D shape, we render motion-blurred images and compare them with the observed ground-truth (GT) images. The shape is then iteratively refined by minimizing the discrepancy between the rendered and GT images. This analysis-by-synthesis approach allows for shape recovery from multi-view blurred images, even under extreme translational and rotational motion.

We evaluate our method on a wide range of testing cases across various shapes and categories. Our method successfully recovers shapes from heavily blurred images caused by ultra-fast motion. Additionally, we demonstrate 3D shape recovery from real-world motion-blurred images, showcasing the effectiveness of our method in challenging real-world scenarios. Our work pushes the boundaries of 3D recovery from ultra-fast motion-blurred images.

## 2. Related Work

### 2.1. General Deblurring Methods

Motion blur arises when multiple scene contents are projected onto the same pixel due to motion during image capture [43]. This blur can originate from various sources, including camera motion, object motion, or long exposures

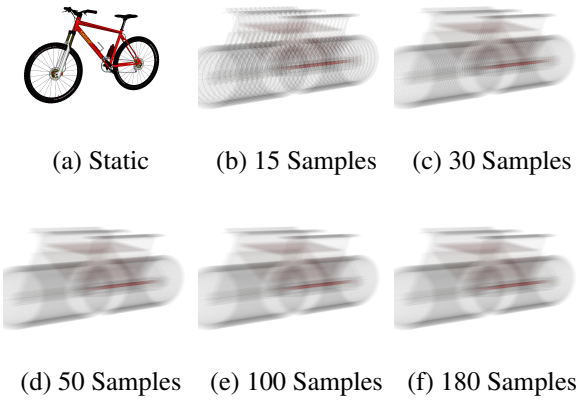

(a) Static (b) 15 Samples (c) 30 Samples

(d) 50 Samples (e) 100 Samples (f) 180 Samples

Figure 2. Motion blur is typically synthesized by rendering and averaging multiple frames. However, for extreme motion, a large number of frames are required to achieve realistic results. Here, we illustrate a bicycle undergoing extreme translation. Noticeable artifacts appear when using fewer samples, and at least 50 frames are needed to produce a realistic motion-blurred image.

in low-light conditions. Typically, motion blur is modeled as a convolution of a clean image with a blur kernel. Numerous methods have been developed to address this issue, leveraging various priors such as total variation (TV) and phase information [27], deep neural networks [12, 13, 26, 36, 44, 45], generative adversarial networks [19, 20, 42], and, more recently, diffusion models [2, 6, 7, 38, 39]. However, these methods primarily focus on low-speed motion, where the blur kernels remain relatively small. Furthermore, most approaches are confined to 2D image space, making them ineffective for handling more complex, non-linear motion patterns, such as rotations.

### 2.2. Shape Recovery from Blurry Images or Videos

Our objective is to recover 3D shapes from blurry images of objects undergoing extremely fast motion [10, 37]. Objects exhibiting motion blur are often categorized as Fast Moving Objects (FMOs) [30]. Prior works have explored reconstructing both shape and motion from images or videos [17, 18, 31]. Rozumnyi et al. [33, 34] pioneered methods to recover 2D and 3D shapes along with motion from blurry images and videos. These approaches effectively leverage neural network-based learned priors, such as the DeFMO network [32], to predict per-timestamp static silhouettes of the object. Combined with differentiable rendering techniques [5, 22], they jointly estimate shape and motion via optimization, enabling robust solutions across a broad range of practical scenarios.

While impressive results are achieved, these methods also largely rely on accurately estimating object motion and static silhouettes, which might struggle with challenging, ultra-fast motion inputs. In this scenario, the resulting blur introduces an unprecedented level of visual ambiguity, making the accurate recovery of static object silhouettes par-

ticularly challenging for [32]. In contrast, our method enables shape recovery under significantly more extreme high-speed motion conditions, demonstrating new capabilities in reconstructing objects undergoing ultra-fast motion.

### 2.3. Inverse Rendering

Shape recovery through inverse rendering has made rapid progress in recent years. A variety of 3D representations, including meshes, neural radiance fields (NeRF) [24], and Gaussian splatting [15], have been combined with differentiable rendering techniques such as mesh rendering [5, 14, 21, 22], volume rendering [8], and surface rendering [28] to jointly estimate shape, texture, lighting, and material directly from images [25, 40]. However, these methods are generally designed for clean, static images, and their applicability to motion-blurred scenes remains limited. In this paper, we propose a differentiable, rasterization-based renderer specifically designed to handle ultra-fast motion. Our approach extends inverse rendering to extreme motion-blurred conditions, making it a promising solution for high-speed shape recovery.

## 3. Method

We now describe our method. We first provide the preliminaries of traditional rasterization algorithms in Sec. 3.1 and analyze their computational bottleneck. We then present our solution: a fast barycentric coordinate solver in Sec. 3.2. With this new solver, we detail our differentiable motion-blur rendering algorithm in Sec. 3.3.

### 3.1. Preliminaries of Rasterization

Rasterization is a fundamental rendering technique that projects 3D triangle meshes onto a 2D image plane. Typically, it operates on a per-pixel basis by computing its barycentric coordinates with respect to each triangle. For a screen pixel $\boldsymbol{p}_i$ and a projected triangle face $\mathbf{F}_j$ with three vertices $\begin{bmatrix}\boldsymbol{v}_0 & \boldsymbol{v}_1 & \boldsymbol{v}_2\end{bmatrix}$, we denote the barycentric coordinates of $\boldsymbol{p}_i$ with respect to $\mathbf{F}_j$ as $\boldsymbol{w} = \begin{bmatrix}w_0 & w_1 & w_2\end{bmatrix}^T$, which satisfies the equation:

$$\boldsymbol{p}_i = w_0\boldsymbol{v}_0 + w_1\boldsymbol{v}_1 + w_2\boldsymbol{v}_2. \tag{1}$$

The vector $\boldsymbol{w}$ is then used to interpolate vertex attributes, such as colors or texture UV mappings.

Traditional differentiable rasterizers (*e.g.*, [5, 22]) compute $\boldsymbol{w}$ by solving a linear system. For example, if we define $\boldsymbol{p}_i = \begin{bmatrix}u & v & 1\end{bmatrix}^T$ and each vertex $\boldsymbol{v} = \begin{bmatrix}x & y & 1\end{bmatrix}^T$, the triangle $\mathbf{F}_j$ can be expressed as:

$$\mathbf{F}_j = \begin{bmatrix} x_0 & x_1 & x_2 \\ y_0 & y_1 & y_2 \\ 1 & 1 & 1 \end{bmatrix}. \tag{2}$$

The barycentric coordinates can then be obtained by solving:

$$\mathbf{F}_j\boldsymbol{w} = \boldsymbol{p}_i \Rightarrow \boldsymbol{w} = \mathbf{F}_j^{-1}\boldsymbol{p}_i. \tag{3}$$

If all $w_0, w_1, w_2$ fall within the range $[0, 1]$, the pixel $\boldsymbol{p}_i$ is covered by the triangle $\mathbf{F}_j$. Its final color is then determined using the Z-buffer algorithm, which selects the closest surface among all overlapping triangles.

**Discussion** We observe that barycentric coordinate computation constitutes a significant computational bottleneck in the context of differentiable motion-blur rasterization. Since barycentric weights for every pixel must be computed with respect to relevant triangles, the cost scales linearly with the number of temporal samples required to generate smooth, realistic blur effects. To overcome this limitation, we propose a fast barycentric coordinate solver that drastically reduces computational complexity and significantly accelerates rendering speed.

### 3.2. Fast Barycentric Coordinate Solver

Traditional rasterization methods [5, 22] synthesize motion blur by rendering multiple $K$ frames and averaging them. However, by assuming that each triangle moves *linearly* in time, we propose a fast barycentric coordinate solver that avoids the heavy cost of repeated $K$ barycentric computation.

Consider a 3D mesh object $M$ moving linearly from time $T = 0$ to $T = 1$, where our goal is to render $K$ frames at time steps $T = \frac{0}{K-1}, \frac{1}{K-1}, \frac{2}{K-1}, \ldots, \frac{K-1}{K-1}$. For a triangle $\mathbf{F}_j$ moving from $T = 0$ to $T = 1$, at a specific time $T = t$, its time-dependent vertex positions can be defined as:

$$\mathbf{F}_j(t) = \begin{bmatrix}\boldsymbol{v}_0(t) & \boldsymbol{v}_1(t) & \boldsymbol{v}_2(t)\end{bmatrix}. \tag{4}$$

Since we assume linear motion, each vertex position follows linear interpolation between the starting point $\boldsymbol{v}(0)$ and ending point $\boldsymbol{v}(1)$:

$$\boldsymbol{v}(t) = (1-t)\boldsymbol{v}(0) + t\boldsymbol{v}(1). \tag{5}$$

Thus, the matrix representation of $\mathbf{F}_j(t)$ can be represented as:

$$\mathbf{F}_j(t) = \begin{bmatrix} x_0(t) & x_1(t) & x_2(t) \\ y_0(t) & y_1(t) & y_2(t) \\ 1 & 1 & 1 \end{bmatrix}. \tag{6}$$

We then compute the barycentric weights $\boldsymbol{w}(t)$ as:

$$\boldsymbol{w}(t) = \mathbf{F}_j(t)^{-1}\boldsymbol{p}_i = \frac{\mathrm{adj}(\mathbf{F}_j(t))}{\det(\mathbf{F}_j(t))}\,\boldsymbol{p}_i, \tag{7}$$

where $\mathrm{adj}(\mathbf{F}_j(t))$ and $\det(\mathbf{F}_j(t))$ are the adjugate matrix and determinant of $\mathbf{F}_j(t)$.

Moreover, with the assumption of linear motion, they could be written as quadratic functions of $t$:

$$\boldsymbol{w}(t) = \frac{\boldsymbol{A}_1 t^2 + \boldsymbol{A}_2 t + \boldsymbol{A}_3}{a_1 t^2 + a_2 t + a_3}, \tag{8}$$

where $\boldsymbol{A}_1, \boldsymbol{A}_2, \boldsymbol{A}_3, a_1, a_2, a_3$ are precomputed $3\times1$ vectors and values that are independent of $t$ and depend solely on $\mathbf{F}_j(0), \mathbf{F}_j(1)$ and $\boldsymbol{p}_i$. Consequently, for the total $K$ frames, these coefficients $(\boldsymbol{A}_1, \boldsymbol{A}_2, \boldsymbol{A}_3, a_1, a_2, a_3)$ can be computed *only once*, and the barycentric coordinate $\boldsymbol{w}(t)$ can then be evaluated using Eq. (8). This allows for efficient barycentric computation without per-frame solving barycentric linear equations. The full derivation is provided in Section B.

### 3.3. Differentiable Rasterization

With our fast solver, we now describe our differentiable motion-blur rasterization, which is built on prior state-of-the-art differentiable rasterization works SoftRas [22] and DIB-R [5].

We first decompose the entire motion into several segments, assuming that inside each segment, all faces move linearly, which is a common assumption in previous motion-blur simulation work [10, 29, 37]. Note that our method can support complex motions, *e.g.*, a motion composed of rotation and translation, as long as it can be divided into linear motion segments (see Sec. L.1). For linear motions, such as translation, larger segments can be used, whereas for non-linear motions, like rotation, smaller segments are employed. In our experiments, we find that even for the extreme rotational motion, we can divide the full rotation into 12 segments and render smooth results.

Next, for each segment, we treat its start and end as keyframes and render intermediate frames with our fast solver. These rendered frames are averaged to generate the segment blurry image. Subsequently, all segment images are further averaged to produce the final blurry image.

Following DIB-R [5], we also separately process *foreground* pixels (covered by one or more faces) and *background* pixels (not covered by any faces) attributes.

**Foreground Pixels** For foreground pixels, we perform barycentric interpolation for each frame at time $T = t$ on the closest covering face using the Z-buffer:

$$I(t) = w_0(t)c_0 + w_1(t)c_1 + w_2(t)c_2, \tag{9}$$

where $c$ represents vertex attributes (*e.g.*, vertex colors or texture UV coordinates).

**Background Pixels** If a pixel is not covered by any triangle, in differentiable rasterization it is assumed that it could be influenced by all triangles. Similarly, we extend the probability of a triangle $\mathbf{F}_j$ influencing a pixel $\boldsymbol{p}_i$ to a time-dependent version:

$$A_i^j(t) = \exp\left(-\frac{d\left(\boldsymbol{p}_i, \mathbf{F}_j(t)\right)}{\delta}\right), \tag{10}$$

where $A_i^j(t)$ is the time-dependent probability, $\delta$ is a hyperparameter [22], and $d\left(\boldsymbol{p}_i, \mathbf{F}_j(t)\right)$ is the squared Euclidean distance, which can be defined as

$$d\left(\boldsymbol{p}_i, \mathbf{F}_j(t)\right) = \min_{\boldsymbol{p}\in\mathbf{F}_j(t)} ||\boldsymbol{p}_i - \boldsymbol{p}||_2^2. \tag{11}$$

The core of the Euclidean distance calculation lies in finding $\boldsymbol{p} \in \mathbf{F}_j(t)$ that is closest to $\boldsymbol{p}_i$. By replacing $\boldsymbol{p}$ with another form $\boldsymbol{p} = \mathbf{F}_j(t)\hat{\boldsymbol{w}}$, where we constrain $\hat{\boldsymbol{w}} \in [0,1]^3$ to ensure $\boldsymbol{p} \in \mathbf{F}_j(t)$, finding the closest $\boldsymbol{p}$ is equivalent to finding $\hat{\boldsymbol{w}}^*$, which can be written as:

$$\hat{\boldsymbol{w}}^* = \arg\min_{\hat{\boldsymbol{w}}\in[0,1]^3} \|\mathbf{F}_j(t)\boldsymbol{w}(t) - \mathbf{F}_j(t)\hat{\boldsymbol{w}}\|_2^2, \tag{12}$$

where we also replace $\boldsymbol{p}_i = \mathbf{F}_j(t)\boldsymbol{w}(t)$.

However, we find that evaluating Equation (12) requires additional computational resources for computing $\mathbf{F}_j(t)$ across frames. To further accelerate the computation, we approximate $\mathbf{F}_j(t)$ with either $\mathbf{F}_j(0)$ or $\mathbf{F}_j(1)$, depending on whether $t$ is closer to the start or the end:

$$\hat{\boldsymbol{w}}^* = \arg\min_{\hat{\boldsymbol{w}}\in[0,1]^3} \|\mathbf{F}_j(X)\boldsymbol{w}(t) - \mathbf{F}_j(X)\hat{\boldsymbol{w}}\|_2^2,\ X = \begin{cases} 0 & t \le 0.5 \\ 1 & t > 0.5 \end{cases} \tag{13}$$

Eq. (13) requires only the evaluation of $\mathbf{F}_j^{(0)}, \mathbf{F}_j^{(1)}$, which significantly reduces computational cost while introducing only minor approximation errors. The full derivation is provided in Sec. B. Finally, with the computed $\hat{\boldsymbol{w}}^*$, we obtain

$$d\left(\boldsymbol{p}_i, \mathbf{F}_j(t)\right) = \|\mathbf{F}_j(t)\boldsymbol{w}(t) - \mathbf{F}_j(t)\hat{\boldsymbol{w}}^*)\|_2^2. \tag{14}$$

We then combine the probabilistic influence of all triangle faces on a particular pixel as

$$A_i(t) = 1 - \prod_j \left(1 - A_i^j(t)\right). \tag{15}$$

**Gradient Computation** Equations (9) and (15) are fully differentiable [5, 22]. Therefore, our method supports backpropagation by propagating gradients through each time-dependent intermediate frame, and ultimately into the keyframes, ensuring efficient optimization in inverse rendering tasks.

## 4. Analysis

In this section, we evaluate the effectiveness of our method through extensive synthetic experiments. We implemented our method based on SoftRas [22] but split the pixels into foreground and background, following DIB-R [5]. We provide the implementation details in Section C.

We first analyze the ultra-fast motion blur synthesis effect in Sec. 4.1, including both forward rendering and backward gradients. Then, in Sec. 4.2, we present the computation speed, demonstrating significant acceleration over prior methods.

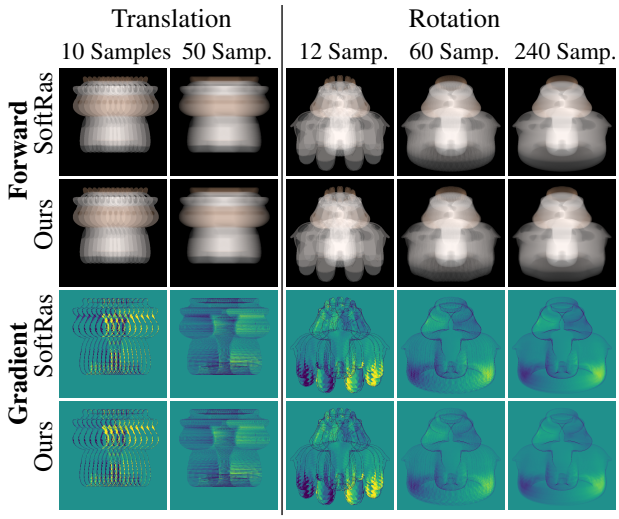


Figure 3. Forward rendering & backward gradient visualization for ultra-fast motion-blur synthesis. Our rendered images and gradients exhibit a high degree of similarity to those generated by SoftRas across various motion cases and sample numbers. Scene settings and render details are provided in Sections E and I.

### 4.1. Qualitative Validation

We first present the synthesis of ultra-fast motion blur effects, including both translational and rotational movements. We show forward rendering results and their backward gradients. As a reference, we also apply SoftRas [22] to render with the same settings (*e.g.*, the same number of sampled frames) and compute the corresponding gradients. The default hyperparameter values provided in SoftRas are used for this comparison.

The comparison results are shown in Fig. 3. Across all test cases, our rendered images and gradients exhibit a high degree of similarity to those generated by SoftRas, which demonstrates the effectiveness of our method in realistic and differentiable motion blur synthesis. In theory, under linear motion, our foreground pixel renderings should be identical to those of SoftRas, whereas our background pixel computation shows slight discrepancies, primarily due to our Euclidean distance approximation (as detailed in Eqs. (12) and (13)). However, we show that these minor discrepancies have negligible impact on gradient computation of our method (Fig. 3 Bottom).

### 4.2. Speed Comparison

Our method is significantly more efficient than traditional blur synthesis methods, *e.g.*, applying SoftRas to render and average multiple frames. To evaluate the running speed, we randomly select 50 models from ShapeNet [3], each containing an average of 5,536 faces. We apply random rotations to each model, render $128 \times 128$ front-view motion-blurred silhouette and color images, and measure the time required for both forward rendering and gradient computation in a single pass. We render objects undergoing linear translation with a varying number of samples. The evaluation considers the average time required for forward rendering and backward gradient computation across all models. All experiments are conducted on a single NVIDIA RTX 4090 GPU with 24GB of memory. More details are provided in Section I.

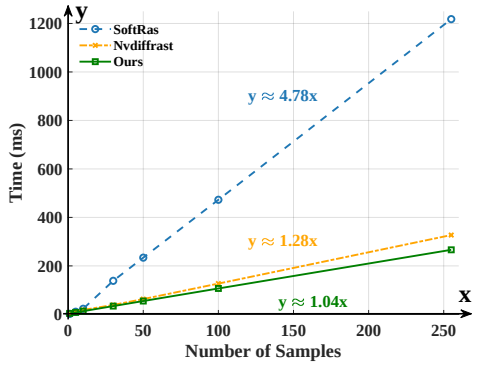


Figure 4. Forward + gradient computation timing results. The slope represents the average time of sampling once, the lower the better. Our method achieves speedups of up to 4.57× and 1.23× compared to SoftRas and Nvdiffrast, respectively.

The timing results are summarized in Fig. 4. Our method achieves speedups of up to 4.57× over SoftRas and 1.23× over Nvdiffrast. Regarding Nvdiffrast [21], it is a highly performant OpenGL-optimized rasterization library, whereas our implementation is built on the SoftRas implementation. Nevertheless, our method is still faster than Nvdiffrast, and incorporating our method into Nvdiffrast would likely bring further acceleration. Moreover, we observe that Nvdiffrast produces weak gradient signals, as its gradients are computed only near edges. This limitation can lead to slower convergence or even failure in extreme shape recovery tasks. In contrast, our method enables global gradient propagation across all triangle primitives, facilitating smoother optimization. Further discussion is provided in Sec. 6.4.

## 5. Shape Optimization from Blurred Images

With our differentiable rendering pipeline, we now present inverse rendering applications, *i.e.*, recovering 3D shapes from ultra-fast motion-blurred images. Thanks to our efficient framework, our method supports rendering more samples, resulting in smoother forward rendering effects and better backward gradients across the optimization process. We demonstrate the effectiveness and advantages of our method through two challenging tasks, where the goals are to recover the 3D shape of ultra-fast moving objects from two representative types of motion blur: multi-view translational and rotational blurred images.

Similar to other inverse rendering tasks, we assume known rendering parameters for each image, including its camera viewpoint and blur settings (translation or rotation speed).

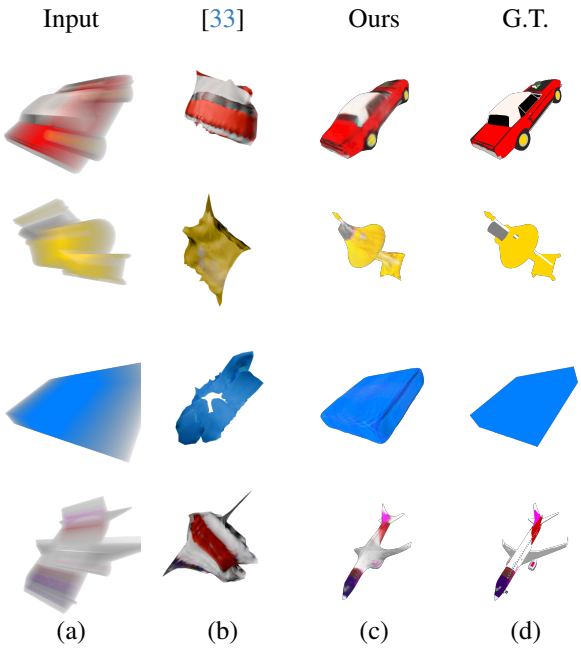


Figure 5. Qualitative results on geometry and color optimization. (a) One of blurred input images. (b) State of the Art [33] result. (c) Our optimization result. (d) Ground-truth object. Our method yields significant superior results than the state-of-the-art work. Note that the object trajectories are synthesized to test the solver's robustness to diverse motion vectors, rather than simulating realistic physical dynamics.

### 5.1. Translational Recovery

We begin with the task of optimizing a 3D shape undergoing linear translation. Given multi-view RGBA translational blurred images (consisting of RGB color $I$ and transparency $\alpha$) as input, our method optimizes a mesh $M$ with vertex positions $V$ and a texture map $C$ such that the rendered images, $\hat{I}, \hat{\alpha} = R(V, C)$, match the input.

The optimization of $V$ and $C$ is performed by minimizing the image loss and regularization terms. We adopt the $\mathcal{L}_1$ loss for both color $I, \hat{I}$ and transparency $\alpha, \hat{\alpha}$, formulated as:

$$\mathcal{L}_{\text{img}} = \left\| I - \hat{I} \right\|_1 + \left\| \alpha - \hat{\alpha} \right\|_1 . \tag{16}$$

Similar to [5, 22], we incorporate a smoothness loss $\mathcal{L}_{\text{s}}$ and a Laplacian loss $\mathcal{L}_{\text{L}}$ to regularize the deformation of $V$ (details provided in Section G). The final loss function is defined as:

$$\mathcal{L} = \mathcal{L}_{\text{img}} + \lambda_{\text{s}}\mathcal{L}_{\text{s}} + \lambda_{\text{L}}\mathcal{L}_{\text{L}}. \tag{17}$$

### 5.2. Rotational Recovery

We further apply our method to a more challenging task: reconstructing fast-rotating objects from motion-blurred images. Similarly, given multi-view images $I$ as input, our method reconstructs a 3D mesh $M$ corresponding to the observed object.

| Method | Translation | | Rotation |
|---|---|---|---|
| | 3D IoU ↑ | Static PSNR ↑ | Blurred PSNR ↑ |
| [33] | 0.152 | 11.63 | 13.58 |
| Ours | 0.679 | 19.20 | 31.89 |

Table 1. Quantitative comparison for shape optimization from blurred images. We compare the best performance between our method and the state-of-the-art [33]. Our method achieves significantly superior performance compared to [33].

Due to the highly non-convex nature of the rotation optimization problem, we observe that directly optimizing mesh vertices rarely yields well-shaped objects (illustrated in Sec. F). To mitigate this issue, we optimize a Signed Distance Function (SDF) representation instead. We construct an SDF field $\mathcal{S}$ following [41], and extract a mesh $M$ using FlexiCubes [35] in a differentiable manner. Our differentiable renderer $R$ is then employed to generate corresponding rotation images $\hat{I}$, which are subsequently used to optimize $\mathcal{S}$ via loss functions. Given the complexity of the SDF representation, we render grayscale images in this setting and focus on shape recovery.

We retain the same $\mathcal{L}_{\text{img}}$ loss (from Eq. (17)) for image consistency. For SDF regularization, we utilize the loss terms $\mathcal{L}_{\text{crit}}$ and $\mathcal{L}_{\text{reg}}$ from [41] and [35], respectively (details in Section G). The final loss function is defined as:

$$\mathcal{L} = \mathcal{L}_{\text{img}} + \lambda_{\text{crit}}\mathcal{L}_{\text{crit}} + \lambda_{\text{reg}}\mathcal{L}_{\text{reg}}. \tag{18}$$

## 6. Experiments

In this section, we present qualitative and quantitative experiments to evaluate the effectiveness and efficiency of our method for shape recovery from ultra-fast motion-blurred images. In Secs. 6.1 and 6.2, we present translational and rotational blurred shape recovery, respectively. Furthermore, we validate our method's practical applicability through real-world motion blur data in Sec. 6.3. Finally, we conduct an ablation study in Sec. 6.4, to demonstrate the benefits of our method compared to the widely adopted codebase SoftRas [22] and Nvdiffrast [21] under extreme motion blur conditions. All hyperparameter settings and more results are provided in Sections I, J and L.

### 6.1. Translational Recovery

In this experiment, we present our method's 3D shape reconstruction performance for objects undergoing translational motion, specifically benchmarking against the state-of-the-art [33]. We perform optimization on 25 selected shapes from ShapeNet, and evaluate both the geometry and color recovery. For geometry quantitative evaluation, we voxelize the predicted and ground truth meshes into $32^3$ volumes, and compute the 3D IoU. For color quantitative evaluation, we compare the PSNR of multi-view static novel-view-synthesis (NVS) of the objects. Quantitative evalua-

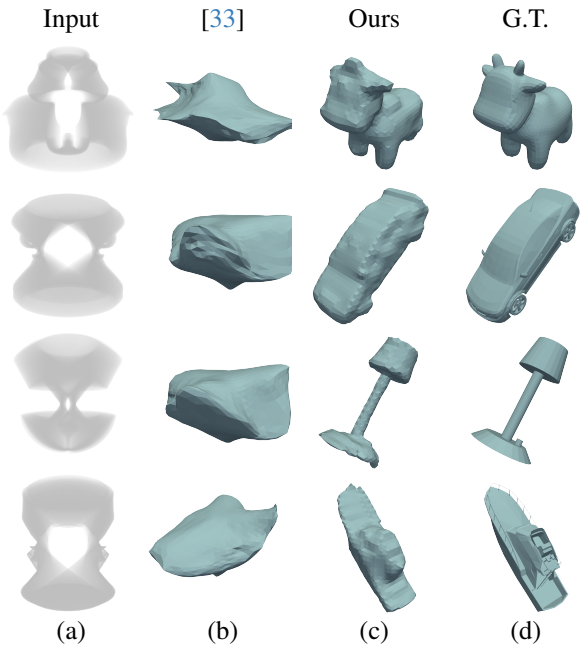


Figure 6. Qualitative results for optimization on rotating objects. (a) One of blurred input images. (b) State of the Art [33] result. (c) Our optimization result. (d) Ground-truth object. Our method also yields a significant superior better than the state-of-the-art work.

tion results are presented in Tab. 1, while qualitative results are illustrated in Fig. 5.

We assess our method's fundamental capability in 3D shape recovery from highly motion-blurred images by benchmarking against the state-of-the-art work [33]. As presented in Tab. 1 and Fig. 5, our method demonstrates a significant advantage in translational recovery. Notably, [33]'s reliance on the learning prior [32] to predict static silhouettes fundamentally limits its performance in the challenging blurry input. In contrast, our method successfully recovers meaningful 3D shape and appearance. More details and analysis are provided in Section K.1.

### 6.2. Rotational Recovery

In this experiment, we evaluate shape recovery for objects undergoing ultra-fast rotational motion, benchmarking against the state-of-the-art [33]. Here, we observe that multiple feasible 3D shape solutions may correspond to the same blurred image; a detailed analysis is provided in Section H. Consequently, traditional 3D evaluation metrics (*e.g.*, 3D IoU, Chamfer Distance) are not suitable. Therefore, we assess the similarity between the rotational-blurred images rendered from the reconstructed objects and the ground truth, quantified using PSNR.

Similar to Sec. 6.1, for rotational motion, a similar trend of superior performance is observed for our method compared to [33]. As shown in Tab. 1 and Fig. 6, our method achieves a significantly superior performance and succeeds in a high-quality 3D reconstructions even under extreme rotational scenarios.

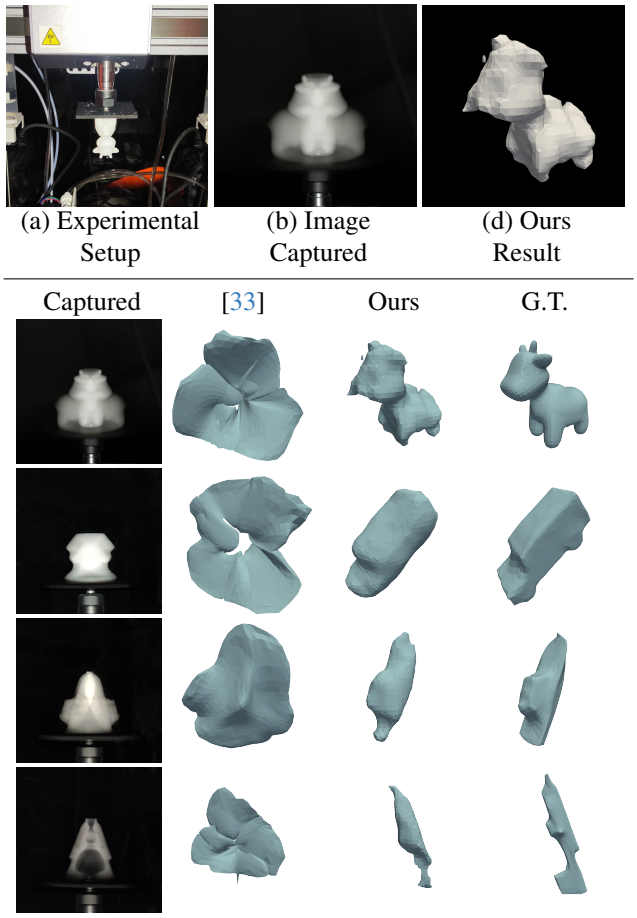


Figure 7. Real-world experiment. (a) Our experimental setup. (b) The original image captured. (c) Ours optimization result. The remaining rows: More real-world examples. Quantitatively, our method achieves a superior blurred PSNR score of 24.52 dB compared to 12.51 dB for [33]. Our method is capable of reconstructing 3D objects from real-world motion-blurred images.

### 6.3. Real-World Results

Next, we evaluate our method on real-world images. We capture a front view of 3D-printed rotating objects at 100 Hz with a camera exposure time of $1/100$ s. Since the data was captured in a controlled studio environment with a black background, we extract the object alpha masks based on pixel intensity thresholds to serve as supervision signals. After preprocessing, including cropping and brightness correction, we perform rotational shape optimization using the same settings as described in Sec. 5.2.

Results and evaluations are presented in Fig. 7. The 3D print technique allows us to establish ground truth for evaluation. As summarized, our method achieves a superior blurred PSNR score of 24.52 dB compared to 12.51 dB for [33], demonstrating a significant improvement. Qualitatively, due to the imperfect pose and noise introduced in real data, the recovered shape exhibits slight artifacts compared

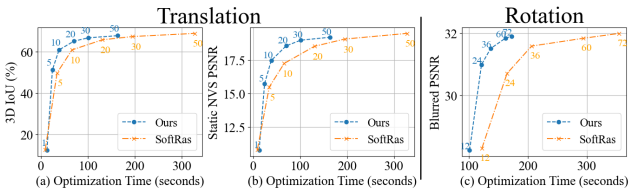


Figure 8. Optimization results for objects undergoing translation and rotation. We draw optimization time v.s. performance curves for our method and SoftRas, where each point indicate different number of samples.

to the synthetic recovery results. Nevertheless, our method successfully recovers reasonable shapes, demonstrating its capability to handle real-world data effectively.

### 6.4. Ablation Study

Finally, we conduct an ablation study to validate our key design choices. Specifically, we analyze the efficiency improvements of our method compared to the codebase SoftRas, and assess the robustness and gradient quality of our method against high-performance Nvdiffrast under the extreme motion blur scenarios.

**Comparison with SoftRas** Our method is built upon the SoftRas framework. Therefore, we compare our method against SoftRas in terms of optimization time and reconstruction quality. As shown in Fig. 8, several interesting points can be observed. First, increasing the number of samples improves performance but also increases optimization time. This is reasonable as more samples result in better blur simulation, yielding better shape recovery performance and longer time. Second, our method exhibits strong efficiency over SoftRas. Given the same number of samples, our method achieves significantly faster optimization time. Conversely, for the same optimization time, our method yields superior reconstruction quality.

**Comparison with Nvdiffrast** Next, we present a comparison of our method's gradient quality and robustness against Nvdiffrast. We first quantitatively assess the convergence behaviors of both methods as a function of the number of iterations. As illustrated in Fig. 9, our method demonstrates a significantly faster convergence rate. This is attributable to the stronger and more stable gradients generated by our approach, in contrast to the comparatively weaker gradients produced by Nvdiffrast.

Beyond convergence speed, we observe that Nvdiffrast [21] frequently encounters catastrophic failures, leading to the inability to reconstruct valid meshes. For example, in our experiments on rotational recovery, Nvdiffrast failed to successfully complete the process (manifested as program crashes) in any of the 10 repeated attempts within 8 out of 25 test data cases, which even precluded a quantitative comparison with our method. Furthermore, even in cases where Nvdiffrast manages to complete the reconstruction, its output quality often exhibits lower fidelity compared to ours,

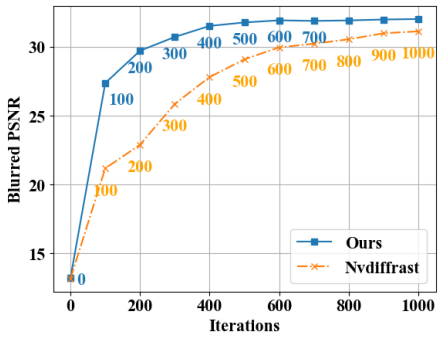


Figure 9. Comparison of convergence rates between our method and Nvdiffrast w.r.t. number of iterations. Labels denote numbers of iterations. The convergence rate of Nvdiffrast is significantly slower than that of our method, which we attribute to its weaker pixel-wise gradients.

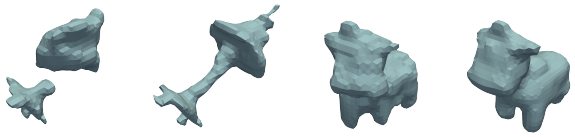

(a) Nvdiffrast (b) Ours (c) Nvdiffrast (d) Ours

Figure 10. Failure cases of Nvdiffrast. (a, c) Nvdiffrast optimization results. (b, d) Ours optimization results. In this task, our method can successfully recover a well-shaped object in most scenarios, whereas Nvdiffrast frequently fails, or producing distorted and uneven objects.

as illustrated in Fig. 10. In stark contrast, our method consistently achieves successful, well-shaped, and high-fidelity reconstructions. More analysis is provided in Section K.2.

## 7. Discussion

**Limitations** Our method currently relies on known camera poses and motion parameters. Additionally, our physical formation model assumes linear motion segments and a linear, noise-free photometric response. While effective, these assumptions may deviate from in-the-wild scenarios characterized by complex non-linear motion, camera response functions (tone mapping), or sensor noise. We provide a comprehensive discussion on these limitations and future works in Sec. M.

**Conclusion** In this paper, we propose a novel inverse rendering approach for 3D shape recovery from ultra-fast motion-blurred images. Our fast barycentric coordinate solver accelerates rendering while preserving accuracy, enabling efficient and fully differentiable shape reconstruction. Experimental results validate the effectiveness of our method on both synthetic and real-world data, advancing 3D reconstruction under ultra-fast motion blur.

## 8. Acknowledgements

This work is supported in part by grants from National Key Research and Development Program of China (Grant No. 2024YFB3309500), National Natural Science Foundation of China (Grant No. U23A20312, 62472257).

## References


[1] Moritz Bächer, Emily Whiting, Bernd Bickel, and Olga Sorkine-Hornung. Spin-it: Optimizing moment of inertia for spinnable objects. *ACM Transactions on Graphics (TOG)*, 33(4):1–10, 2014. 1

[2] Weimin Bai, Siyi Chen, Wenzheng Chen, and He Sun. Blind inversion using latent diffusion priors. *arXiv preprint arXiv:2407.01027*, 2024. 2

[3] Angel X Chang, Thomas Funkhouser, Leonidas Guibas, Pat Hanrahan, Qixing Huang, Zimo Li, Silvio Savarese, Manolis Savva, Shuran Song, Hao Su, et al. Shapenet: An information-rich 3d model repository. *arXiv preprint arXiv:1512.03012*, 2015. 5

[4] Wenbo Chen and Ligang Liu. Deblur-gs: 3d gaussian splatting from camera motion blurred images. *Proceedings of the ACM on Computer Graphics and Interactive Techniques*, 7 (1):1–15, 2024. 1

[5] Wenzheng Chen, Huan Ling, Jun Gao, Edward Smith, Jaako Lehtinen, Alec Jacobson, and Sanja Fidler. Learning to predict 3d objects with an interpolation-based differentiable renderer. In *NeurIPS*, 2019. 1, 2, 3, 4, 6

[6] Hyungjin Chung, Jeongsol Kim, Michael T Mccann, Marc L Klasky, and Jong Chul Ye. Diffusion posterior sampling for general noisy inverse problems. *arXiv preprint arXiv:2209.14687*, 2022. 2

[7] Hyungjin Chung, Jeongsol Kim, Sehui Kim, and Jong Chul Ye. Parallel diffusion models of operator and image for blind inverse problems. In *Proceedings of the IEEE/CVF Conference on Computer Vision and Pattern Recognition*, pages 6059–6069, 2023. 2

[8] Robert A Drebin, Loren Carpenter, and Pat Hanrahan. Volume rendering. *ACM Siggraph Computer Graphics*, 22(4): 65–74, 1988. 3

[9] Yasutaka Furukawa, Carlos Hernández, et al. Multi-view stereo: A tutorial. *Foundations and Trends® in Computer Graphics and Vision*, 9(1-2):1–148, 2015. 1

[10] Carl Johan Gribel, Michael C Doggett, and Tomas Akenine-Möller. Analytical motion blur rasterization with compression. *High Performance Graphics*, 10, 2010. 2, 4

[11] Richard Hartley and Andrew Zisserman. *Multiple view geometry in computer vision*. Cambridge university press, 2003. 1

[12] Meiguang Jin, Givi Meishvili, and Paolo Favaro. Learning to extract a video sequence from a single motion-blurred image. In *Proceedings of the IEEE Conference on Computer Vision and Pattern Recognition*, pages 6334–6342, 2018. 2

[13] Meiguang Jin, Zhe Hu, and Paolo Favaro. Learning to extract flawless slow motion from blurry videos. In *Proceedings of the IEEE/CVF conference on computer vision and pattern recognition*, pages 8112–8121, 2019. 2

[14] Hiroharu Kato, Yoshitaka Ushiku, and Tatsuya Harada. Neural 3d mesh renderer. In *Proceedings of the IEEE conference on computer vision and pattern recognition*, pages 3907–3916, 2018. 1, 3

[15] Bernhard Kerbl, Georgios Kopanas, Thomas Leimkühler, and George Drettakis. 3d gaussian splatting for real-time radiance field rendering. *ACM Transactions on Graphics (ToG)*, 42(4):1–14, 2023. 3

[16] Diederik P Kingma and Jimmy Ba. Adam: A method for stochastic optimization. *arXiv preprint arXiv:1412.6980*, 2014. 5

[17] Jan Kotera, Denys Rozumnyi, Filip Sroubek, and Jiri Matas. Intra-frame object tracking by deblatting. In *Proceedings of the IEEE/CVF International Conference on Computer Vision Workshops*, pages 0–0, 2019. 2

[18] Jan Kotera, Jiří Matas, and Filip Šroubek. Restoration of fast moving objects. *IEEE Transactions on Image Processing*, 29:8577–8589, 2020. 2

[19] Orest Kupyn, Volodymyr Budzan, Mykola Mykhailych, Dmytro Mishkin, and Jiří Matas. Deblurgan: Blind motion deblurring using conditional adversarial networks. In *Proceedings of the IEEE conference on computer vision and pattern recognition*, pages 8183–8192, 2018. 2

[20] Orest Kupyn, Tetiana Martyniuk, Junru Wu, and Zhangyang Wang. Deblurgan-v2: Deblurring (orders-of-magnitude) faster and better. In *Proceedings of the IEEE/CVF International Conference on Computer Vision (ICCV)*, 2019. 2

[21] Samuli Laine, Janne Hellsten, Tero Karras, Yeongho Seol, Jaakko Lehtinen, and Timo Aila. Modular primitives for high-performance differentiable rendering. *ACM Transactions on Graphics (ToG)*, 39(6):1–14, 2020. 3, 5, 6, 8

[22] Shichen Liu, Tianye Li, Weikai Chen, and Hao Li. Soft rasterizer: A differentiable renderer for image-based 3d reasoning. *The IEEE International Conference on Computer Vision (ICCV)*, 2019. 1, 2, 3, 4, 5, 6

[23] Yiren Lu, Yunlai Zhou, Disheng Liu, Tuo Liang, and Yu Yin. Bard-gs: Blur-aware reconstruction of dynamic scenes via gaussian splatting. In *Proceedings of the Computer Vision and Pattern Recognition Conference*, pages 16532–16542, 2025. 1

[24] B Mildenhall, PP Srinivasan, M Tancik, JT Barron, R Ramamoorthi, and R Ng. Nerf: Representing scenes as neural radiance fields for view synthesis. In *European conference on computer vision*, 2020. 3

[25] Jacob Munkberg, Jon Hasselgren, Tianchang Shen, Jun Gao, Wenzheng Chen, Alex Evans, Thomas Müller, and Sanja Fidler. Extracting Triangular 3D Models, Materials, and Lighting From Images. In *Proceedings of the IEEE/CVF Conference on Computer Vision and Pattern Recognition (CVPR)*, pages 8280–8290, 2022. 3

[26] Jinshan Pan, Haoran Bai, and Jinhui Tang. Cascaded deep video deblurring using temporal sharpness prior. In *Proceedings of the IEEE/CVF conference on computer vision and pattern recognition*, pages 3043–3051, 2020. 2

[27] Liyuan Pan, Richard Hartley, Miaomiao Liu, and Yuchao Dai. Phase-only image based kernel estimation for single image blind deblurring. In *Proceedings of the IEEE/CVF conference on computer vision and pattern recognition*, pages 6034–6043, 2019. 2

[28] Hanspeter Pfister, Matthias Zwicker, Jeroen Van Baar, and Markus Gross. Surfels: Surface elements as rendering primitives. In *Proceedings of the 27th annual conference on Computer graphics and interactive techniques*, pages 335–342, 2000. 3

[29] Mads JL Rønnow, Ulf Assarsson, and Marco Fratarcangeli. Fast analytical motion blur with transparency. *Computers & Graphics*, 95:36–46, 2021. 4

[30] Denys Rozumnyi, Jan Kotera, Filip Sroubek, Lukas Novotny, and Jiri Matas. The world of fast moving objects. In *Proceedings of the IEEE Conference on Computer Vision and Pattern Recognition*, pages 5203–5211, 2017. 2

[31] Denys Rozumnyi, Jan Kotera, Filip Sroubek, and Jiri Matas. Sub-frame appearance and 6d pose estimation of fast moving objects. In *Proceedings of the IEEE/CVF Conference on Computer Vision and Pattern Recognition*, pages 6778–6786, 2020. 2

[32] Denys Rozumnyi, Martin R Oswald, Vittorio Ferrari, Jiri Matas, and Marc Pollefeys. Defmo: Deblurring and shape recovery of fast moving objects. In *Proceedings of the IEEE/CVF Conference on Computer Vision and Pattern Recognition*, pages 3456–3465, 2021. 1, 2, 3, 7, 5, 6

[33] Denys Rozumnyi, Martin R Oswald, Vittorio Ferrari, and Marc Pollefeys. Shape from blur: Recovering textured 3d shape and motion of fast moving objects. *Advances in Neural Information Processing Systems*, 34:29972–29983, 2021. 2, 6, 7, 5, 8

[34] Denys Rozumnyi, Martin R Oswald, Vittorio Ferrari, and Marc Pollefeys. Motion-from-blur: 3d shape and motion estimation of motion-blurred objects in videos. In *Proceedings of the IEEE/CVF Conference on Computer Vision and Pattern Recognition*, pages 15990–15999, 2022. 2

[35] Tianchang Shen, Jacob Munkberg, Jon Hasselgren, Kangxue Yin, Zian Wang, Wenzheng Chen, Zan Gojcic, Sanja Fidler, Nicholas Sharp, and Jun Gao. Flexible isosurface extraction for gradient-based mesh optimization. *ACM Trans. Graph.*, 42(4), 2023. 6, 3, 4, 5

[36] Wang Shen, Wenbo Bao, Guangtao Zhai, Li Chen, Xiongkuo Min, and Zhiyong Gao. Blurry video frame interpolation. In *Proceedings of the IEEE/CVF conference on computer vision and pattern recognition*, pages 5114–5123, 2020. 2

[37] Konstantin Shkurko, Cem Yuksel, Daniel Kopta, Ian Mallett, and Erik Brunvand. Time interval ray tracing for motion blur. *IEEE transactions on visualization and computer graphics*, 24(12):3225–3238, 2017. 2, 4

[38] Bowen Song, Soo Min Kwon, Zecheng Zhang, Xinyu Hu, Qing Qu, and Liyue Shen. Solving inverse problems with latent diffusion models via hard data consistency. *arXiv preprint arXiv:2307.08123*, 2023. 2

[39] Radim Spetlik, Denys Rozumnyi, and Jiří Matas. Single-image deblurring, trajectory and shape recovery of fast moving objects with denoising diffusion probabilistic models. In *Proceedings of the IEEE/CVF Winter Conference on Applications of Computer Vision*, pages 6857–6866, 2024. 2

[40] Peng Wang, Lingjie Liu, Yuan Liu, Christian Theobalt, Taku Komura, and Wenping Wang. Neus: Learning neural implicit surfaces by volume rendering for multi-view reconstruction. *NeurIPS*, 2021. 3

[41] Zixiong Wang, Yunxiao Zhang, Rui Xu, Fan Zhang, Peng-Shuai Wang, Shuangmin Chen, Shiqing Xin, Wenping Wang, and Changhe Tu. Neural-singular-hessian: Implicit neural representation of unoriented point clouds by enforcing singular hessian. *ACM Transactions on Graphics (TOG)*, 42 (6):1–14, 2023. 6, 4

[42] Kaihao Zhang, Wenhan Luo, Yiran Zhong, Lin Ma, Bjorn Stenger, Wei Liu, and Hongdong Li. Deblurring by realistic blurring. In *Proceedings of the IEEE/CVF conference on computer vision and pattern recognition*, pages 2737–2746, 2020. 2

[43] Kaihao Zhang, Wenqi Ren, Wenhan Luo, Wei-Sheng Lai, Björn Stenger, Ming-Hsuan Yang, and Hongdong Li. Deep image deblurring: A survey. *International Journal of Computer Vision*, 130(9):2103–2130, 2022. 1, 2

[44] Zhihang Zhong, Ye Gao, Yinqiang Zheng, and Bo Zheng. Efficient spatio-temporal recurrent neural network for video deblurring. In *Computer Vision–ECCV 2020: 16th European Conference, Glasgow, UK, August 23–28, 2020, Proceedings, Part VI 16*, pages 191–207. Springer, 2020. 2

[45] Shangchen Zhou, Jiawei Zhang, Jinshan Pan, Haozhe Xie, Wangmeng Zuo, and Jimmy Ren. Spatio-temporal filter adaptive network for video deblurring. In *Proceedings of the IEEE/CVF international conference on computer vision*, pages 2482–2491, 2019. 2